JTTEE5 21:950–962
DOI: 10.1007/s11666-012-9780-z
1059-9630/$19.00 © ASM International

Optimizing Compliance and Thermal Conductivity of Plasma Sprayed Thermal Barrier Coatings via Controlled Powders and Processing Strategies

Yang Tan, Vasudevan Srinivasan, Toshio Nakamura, Sanjay Sampath, Pierre Bertrand, and Ghislaine Bertrand

(Submitted November 19, 2011; in revised form January 30, 2012)

The properties and performance of plasma-sprayed thermal barrier coatings (TBCs) are strongly dependent on the microstructural defects, which are affected by starting powder morphology and processing conditions. Of particular interest is the use of hollow powders which not only allow for efficient melting of zirconia ceramics but also produce lower conductivity and more compliant coatings. Typical industrial hollow spray powders have an assortment of densities resulting in masking potential advantages of the hollow morphology. In this study, we have conducted process mapping strategies using a novel uniform shell thickness hollow powder to control the defect microstructure and properties. Correlations among coating properties, microstructure, and processing reveal feasibility to produce highly compliant and low conductivity TBC through a combination of optimized feedstock and processing conditions. The results are presented through the framework of process maps establishing correlations among process, microstructure, and properties and providing opportunities for optimization of TBCs.

Keywords hollow powder, nonlinear elastic property, plasma-spray processing, thermal barrier coatings

1. Introduction

Plasma-sprayed yttria-stabilized zirconia (YSZ) continues to be material of choice for thermal barrier coatings (TBCs) in advanced gas turbine systems (Ref 1-6). YSZ TBCs offer numerous advantages including low intrinsic thermal conductivity, low coefficient of thermal expansion (CTE) mismatch with the substrate, enhanced toughness, ease-in-processing, established infrastructures, and cost effectiveness. A key factor in the success of plasma-sprayed TBCs is the further decreasing of the already low intrinsic thermal conductivity of YSZ through the process-induced incorporation of pores and interfaces to as small as 40% of bulk value (Fig. 1) (Ref 7-10). These defects also provide the necessary compliance for the survivability of the ceramic coating on a metallic alloy substrate during high temperature thermal cycling (Ref 11).

The evolution of gas turbine technology in recent years has pushed the turbine inlet operational temperature and increased requirements for thermal shielding of the thermal barrier system. In the past, TBCs played the role of life extension of the superalloy component and, as such, were not subject to stringent performance reliability requirements. The situation is changing rapidly. As the inlet temperatures are increased, there is a need for TBCs to become prime reliant rather than just life extension components. In this context, there has been significant growth of research activities related to atmospheric plasma spray (APS) TBC materials, processing, properties, and performance. To achieve the goal of prime reliant APS TBCs, three requirements need to be met concurrently.

1. TBC top coat must be engineered to meet requisite performance goals in terms of thermal shielding, durability and reliability.
2. TBC deposition process must satisfy the microstructure-property requirement and do so reliably.
3. The failure mechanisms of the TBCs must be understood to enable life prediction and associated system prognostics.

Clearly these are intertwined in many ways and the aforementioned aspects are major areas of active research in both academia and industry. Ability to tailor optimal microstructure, which results in desired performance and durability, is a necessary first step in achieving this goal. This study will address recent advances in this arena.

Past work has demonstrated the strong dependence of microstructure (and properties) of plasma-sprayed YSZ

Yang Tan, Vasudevan Srinivasan, Toshio Nakamura, and **Sanjay Sampath**, Center for Thermal Spray Research, Stony Brook University, Stony Brook, NY 11794-2275; and **Pierre Bertrand** and **Ghislaine Bertrand**, Laboratoire d'Etudes et de Recherches sur les Materiauz les Procedes et les Surfaces (LERMPS), Universite de Technologie Belfort-Montbeliard (UTBM), 90010 Belfort, France. Contact e-mails: yangtan@gmail.com and sanjay.sampath@stonybrook.edu.

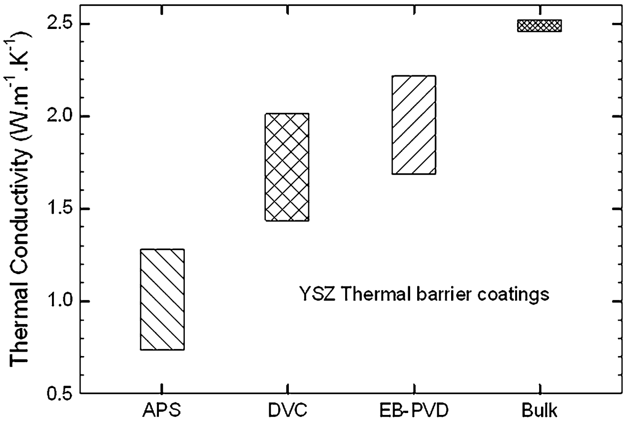

Fig. 1 Typical thermal conductivity of YSZ-based TBCs. APS, atmospheric plasma spray; DVC, dense vertically cracked plasma spray; EB-PVD, electron beam physical vapor deposition)

on the feedstock material characteristics as well as plasma spray process conditions (Ref 12-14). In industry at least three morphologies of YSZ spray particles are used in production of APS TBC systems. They include fused and crushed (FC) powders which are in the form of dense angular particles, agglomerated and sintered (AS) materials which are comprised spray-dried agglomerates of very fine particles followed by dewaxing and sintering, and finally a hollow sphere type powders (HOSP) which are produced by plasma spray alloying and densification of the spray-dried agglomerate. The HOSP material comprises of a spherical shell of YSZ with a hollow core.

It is anecdotally appreciated that coatings produced using HOSP display lower thermal conductivity and enhanced compliance compared to those produced with either FC or AS despite containing similar overall porosity. Kulkarni et al. and Allen et al. have contributed to the understanding of coating microstructure using advanced small angle neutron scattering technique and have attributed this difference to the larger fraction of interlamellar pores in coatings produced from HOSP powders, which leads to enhanced phonon scattering in the through-thickness direction (Ref 15). Image analysis also confirmed these findings. Wang et al. in a subsequent study showed that coatings produced from HOSP materials display a larger fraction of splat-splat interfaces for the same unit thickness of the coating (Ref 16). This can be rationalized as follows: the HOSP material represents a smaller mass for the same volume of the powder particle and as such smaller splat thickness. It has also shown a lower rate of sintering during sustained exposure which was attributed not only to the interlamellar porosity but also due to the larger opening dimensions of the pores and interfaces (as evidenced by neutron scattering results). Detailed evaluation of microstructure-thermal conductivity relationships of APS coatings produced from various powder morphologies have recently been reported by Chi et al. (Ref 17) and points to both lower initial and post-exposure thermal conductivity of the HOSP coatings. The lower sintering rate of the HOSP material was further demonstrated, using Larson-Miller parameter, which was originally used for creep stress-rupture, but has been introduced to describe ‘‘creep-like’’ increase of TBC thermal conductivity due to sintering (Ref 11, 18-20). These attributes have made the HOSP powder more appealing at least for situations requiring low thermal conductivity and reduced sintering rate. FC material is still favored when denser and more erosion resistant coatings are required.

Key powder particle characteristics—particle density and uniformity of wall/shell thickness as well as their distributions in the powder—introduce significant local variations in the microstructure preventing effective utilization of the novel morphology for microstructural tailoring. Recognizing this variability, Bertrand et al. manufactured HOSP powders with uniform particle wall thickness through careful control of spray drying procedures (Ref 21-23). It is further demonstrated that as-sprayed coatings achieved thermal conductivity at or below 1 W/m · K through the combination of the new powders and process parameters (Ref 13). Again, this was attributed to the larger presence of planar interfaces which limited the thermal transport in the system.

In addition to the generally lower thermal conductivity, prior work has also shown that the HOSP coatings are more mechanically compliant than those made from other powders. In general, lower elastic modulus of the HOSP sprayed coating was reported from indentation and 4-point bending tests. Recent work has shown that the HOSP coatings also display a significantly larger nonlinear elastic and hysteretic (collectively termed as anelastic) behavior compared to those of FC and AS materials. Liu et al. (Ref 24) have quantified these nonlinear characteristics through cycling of sprayed coatings with simultaneous measurements of substrate curvature and temperature. The nonlinearity is attributed to pore opening and closing during thermo-mechanical loading while the hysteresis stems from the frictional sliding along weak interfaces and micro-crack surfaces. The HOSP coating with its larger densities of intersplat interfaces and intrasplat cracks tend to exhibit greater nonlinearity and hysteresis. Furthermore, it was shown that anelastic response can be manipulated through processing conditions for the various powder morphologies. However, the large distribution of ‘‘hollowness’’ in the commercial HOSP powder may obscure some of these effects.

The above studies pointed to the potential of combining carefully prepared hollow powders with optimized process conditions to meet the dual requirements of low thermal conductivity and enhanced thermo-mechanical compliance. Furthermore, recent advancements in process science, feedback control, and in situ monitoring of curvature during and after deposition will allow synthesis of comprehensive process maps for plasma spraying of TBCs (Ref 12). This paper addresses this successive strategy: Optimized coatings with controlled microstructure for enhanced compliance, lower thermal conductivity, and improved resistance to sintering.

The specific goal of this investigation is to integrate developments in controlled powder synthesis, process maps, nonlinear elastic measurements, and detailed characterization of thermal conductivity towards achieving optimal thermal conductivity and compliance of APS TBCs. Although this initial work was conducted for YSZ, it is envisioned that concepts presented here will pave the way for the development of new generation of controlled TBC microstructures with implications for enhanced performance.

2. Materials and Methods

2.1 Feedstock Materials

It has been shown in earlier studies that the morphology of the spray-dried granules can be controlled by careful control of slurry characteristics using critical parameters such as amount of dispersant, binder content, and the pH of the slurry (Ref 21-23). Utilizing this understanding, spherical YSZ hollow powders with controlled shell thickness and size distribution ranging from 30 to 155 µm (with d50 of about 90 µm) have been produced at LERMPS laboratory at Universite de Technologie Belfort-Montbeliard (UTBM) in France, using an optimized and controlled spray drying process followed by sintering (3 h at 250 °C then 20 h at 1050 °C) and then sieved. Figure 2 compares the results of this new powder with those of commercially obtained HOSP powders

The hollow powder produced in the laboratory shows an extremely low density of 0.36 g/cm^3 (tap density of 0.44 g/cm^3) for a size distribution ranging from 80 to 100 µm (with d50 around 93 µm) as compared to 3 g/cm^3 (tap density 3.39 g/cm^3) for a agglomerated and sintered YSZ powder (HC Starck AMPERIT 825.092) or even 1.85 g/cm^3 (tap density 2.06 g/cm^3) for a commercial HOSP powder (204NS Sulzer Metco). Although a very few dense particles can be observed (Fig. 2), the hollow spray-dried powder shape produced for this study is relatively homogeneous with a shell thickness to radius ratio of about 0.1 (i.e., a 100 µm in diameter particle has a shell thickness of 5 µm).

2.2 Design of Experiments (DoE), Diagnostics, and Synthesis of Maps

For all the APS experiments reported in this study, a Sulzer Metco 7 MB plasma torch was used with laminar flow of N_2-H_2 gases. Nozzle with 8 mm diameter orifice was used and powder was externally injected using a powder port with 1.8 mm diameter orifice mounted radial to the plasma plume. Powder was fed into the plasma

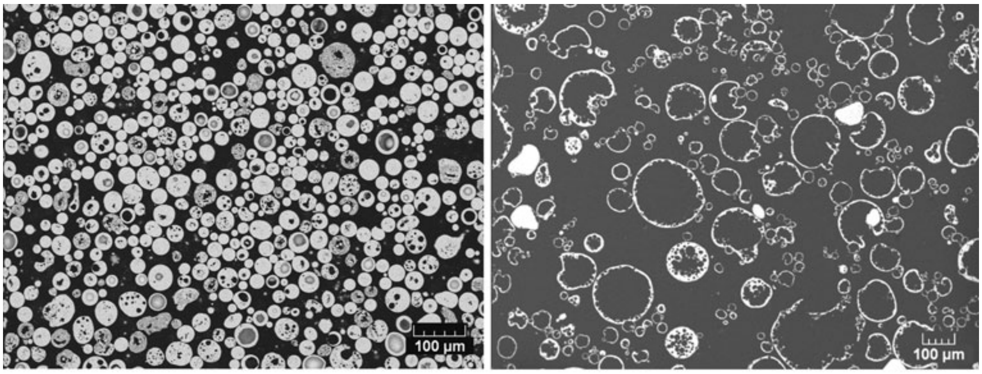

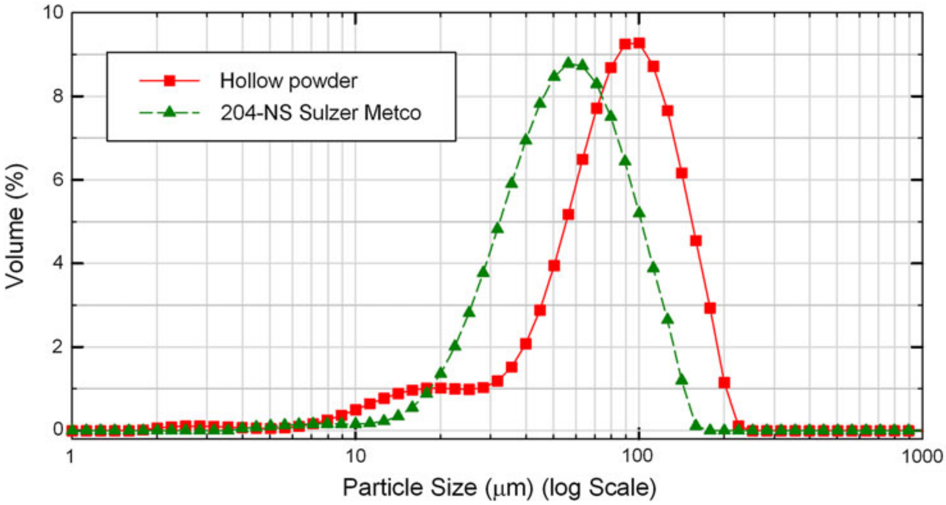

Fig. 2 Feedstock powder cross section images (left, commercially obtained HOSP powder Sulzer Metco 204-NS; right, hollow powder) and comparison of particle size distribution of the two powders. Note that the commercial powders have different levels of particle densities manifested by their variability in ‘‘hollowness’’

using a Sulzer Plasma Technik Twin-10 powder feeding system and the torch was manipulated using a GMC Fanuc S400 six-axis robot. All plasma-spray experiments were conducted at the Center for Thermal Spray Research at Stony Brook University (Table 1).

Developing process maps entails subjecting the material through a controlled set of process conditions through a DoE strategy (Ref 25). To accomplish this, a central composite design was set-up with three main process variables: total mass flow of plasma gases ($N_2 + H_2$), volume ratio of H_2 with respect to the primary gas, and gun current. *JMP IN* software (Release 5.1, SAS Institute Inc., Cary, NC) was used to construct the DoE and to establish quantitative relations between torch parameters and particle state. Details of the procedure are discussed in a Ref 26.

For each spray condition, particle injection was optimized by adjusting the carrier gas flow to control the spray stream trajectory along a predetermined angle. This procedure ensures maximum thermal and kinetic energy (KE) transfer to particles that is representative of the spray condition (without the influence of particle injection parameters such as carrier gas flow) (Ref 27, 28).

Detailed particle diagnostics were conducted for each condition using DPV-2000 particle diagnostic system (Tecnar Automation, Montreal, Canada). Simultaneous measurement of temperature, velocity, and size of individual particles in the spray stream are made for about 10,000 particles in the spray stream flow center for each process condition. Spray stream cross-sectional scans were also performed for each process condition using a 7 × 7 array of locations covering the spray stream (49 equi-spaced points with 5 mm separation) measuring about 300 particles at each location. All measurements were made at a spray distance of 130 mm which was kept constant throughout this investigation.

2.3 Measurement Methodologies and Coating Characterization

2.3.1 Mechanical Properties. Deposits were made on grit-blasted Al 6061 T6511 substrates, 225 × 25 × 3 mm mounted on the *in-situ coating property* (ICP) *sensor*. ICP sensor consists of noncontact displacement lasers and thermocouples to monitor the displacement and temperature, simultaneously, at the back of the sample during spraying and during the subsequent heat-cool cycle. The sample is supported by knife-edge supports to allow for free bending. The in-plane elastic moduli have been calculated from the curvature data using a procedure established by Matejicek and Sampath (Ref 29) based on bi-material bending beam formulations and applied to thermal spray coatings by Tsui and Clyne (Ref 30). Nonlinear stress-strain profiles and the extent of nonlinearity were determined from the curvature-temperature data obtained from post-spray *ex-situ coating property* (ECP) *sensor* (Ref 24). The hysteresis was also studied by examining both the loading and the unloading parts of stress strain relations.

2.3.2 Microstructure and Porosity Analysis. In order to obtain accurate representations of TBC coating porous network, both cutting and polishing steps are carefully conducted. Low cutting speeds are preferred as well as a multistage polishing procedure including pre-polishing with decreasing grade of SiC papers, polishing with decreasing size of diamond pastes (9, 3, and 1 µm, respectively) and finishing with a 0.25 µm diamond paste. TBC polished cross sections were observed by scanning electron microscopy (SEM) in the backscattered electron mode implementing a JSM 5800LV (JEOL SAS, Croissy-sur-Seine, France) as to enhance the contrast between pores and material. A series of 15 images with a resolution of about 0.13 µm/pixel was recorded to get representative porosity values with a standard deviation as low as 1%. Image analysis was implemented to characterize the porous network and detailed information about the image analysis procedure can be found in earlier work (Ref 13, 31). According to this procedure, large pores consisting in globular, elongated, or thick cracks are depicted as macropores, while small pores and thin microcracks are considered as micropores. The porous network is quantitatively described by total porosity, which is the summation of macroporosity (large and globular pores) and microporosity (interlamellar pores and cracks), and total crack length oriented below 30°. These criteria have been found helpful to describe finely cracked coatings containing multi-scaled defects. Details of this method has been introduced in the Materials and Methods section and referred to prior work.

Table 1 Details of DoE for selection of a range of plasma spraying parameters to produce coatings with a range of microstructures

Designator	DoE matrix	N_2 flow (SLM)	H_2 flow (SLM)	Current, A	Voltage, V	Carrier gas flow (SLM)	Coating or not
E1	0 0 0	47.6	5.6	550	81.4	4.8	Yes
E2	a a a	63.1	12.0	634	89.2	5.9	Yes
E3	−a −a −a	31.9	1.7	466	67.2	2.7	Yes
E4	a −a −a	63.8	3.4	466	77.4	5.0	Yes
E5	a a −a	63.1	12.0	466	89.6	5.0	Yes
E6	−a a a	31.6	6.0	634	78.8	3.0	Yes
E7	a −a a	63.8	3.4	634	78.6	5.7	No
E8	−a a −−a	31.6	6.0	466	78.7	2.7	No
E9	−a −a a	31.9	1.7	634	67.2	3.0	No

The 000 represents the center condition of the DoE, while the a a a represents the maximum in parameters space and −a −a −a representing minimum in the parameter matrix

2.3.3 Thermal Conductivity and Aging Effects. Thermal conductivity of the coatings was measured using laser flash system at both room (Holometrix, now part of Netzsch Instruments, Burlington, MA) and elevated temperatures (Flashline-5000, Anter Corporation, Pittsburgh, PA). Free-standing specimens with a diameter of 12.7 mm and thicknesses in the range of 300-500 μm were prepared by separating the coating from the substrate by grinding. Additional to the as-sprayed coatings, the samples were also heat treated with both isothermal (10 h at 1200 °C) and cyclic (20 cycles, 30 min heating at 1100 °C and 15 min cooling for each cycle) exposures, respectively. The thermal conductivity after heat treatment was also measured.

Due to the heterogeneity and anisotropy of the sprayed microstructure, measurement of thermal and in particular nonlinear elastic properties of plasma sprayed coatings is a challenging task. When traditional techniques of property measurement are adapted for plasma-sprayed coatings, there are generally higher uncertainties associated with roughness, specimen preparation, and geometry. For thermal conductivity measurement, laser flash method is suitable for free-standing coating samples, and repeated measurements indicated that the measurement uncertainty is about 5% for each specimen (Ref 20). For microstructure analysis by image analysis, the difficulty is that the void defects exist in multi-scales and very fine features are not discernible. However, consistency in image acquisition and analysis can lead to improvement of the accuracy, which has been demonstrated both by academia and industry for quality assurance of coatings. In general, image analysis gives uncertainty of 5-10% in quantitative estimation of porosity (Ref 13, 32). For mechanical characterizations, the novel bi-layer curvature measurement via thermal cycling maintains the integrity of coating-substrate systems with relatively large specimen dimensions. This technique provides the advantage of a volume averaged measurements of elastic properties over a range of strains with measurement uncertainties <5% (Ref 24, 33, 34).

3. Results and Discussion

3.1 First-Order Process Maps with Controlled Powders

A first-order process map provides relationship between the torch processing conditions and the in-flight particle temperature and velocity (*T*-*V*). This allows characterization of the spray stream and enables relevant parameter selection for process control. The linkage to coating properties is established through the spray stream optimization and referred to as a second-order process map. Detailed process maps have been established for commercially available YSZ materials and reported earlier (Ref 12). The specific goal here is to examine how such maps can be used to tailor microstructures and properties with novel powders.

Figure 3 provides information about in-flight particle temperature and velocity (*T*-*V*) monitored by DPV2000 generated from the DoE. A total of 9 conditions were monitored including ‘‘center’’ condition E1 (000 of the DoE). The left graph in Fig. 3 is showing a typical first-order process map plotting average temperature and velocity gathered from about 10,000 particles at each condition. The average temperature ranged from 2787 to 2932 °C (range 145 °C; 5% of condition E1) and average velocity ranged from 82 to 197 m/s (range 115 m/s; 80% of condition E1). Condition E2 displays the largest values for both *T* and *V*, due to its high torch current and high total gas flow.

A more informative in-fight particle-state parameters are the *T* and *V* distribution based on individual particle state. The two graphs on the right of Fig. 3 show the

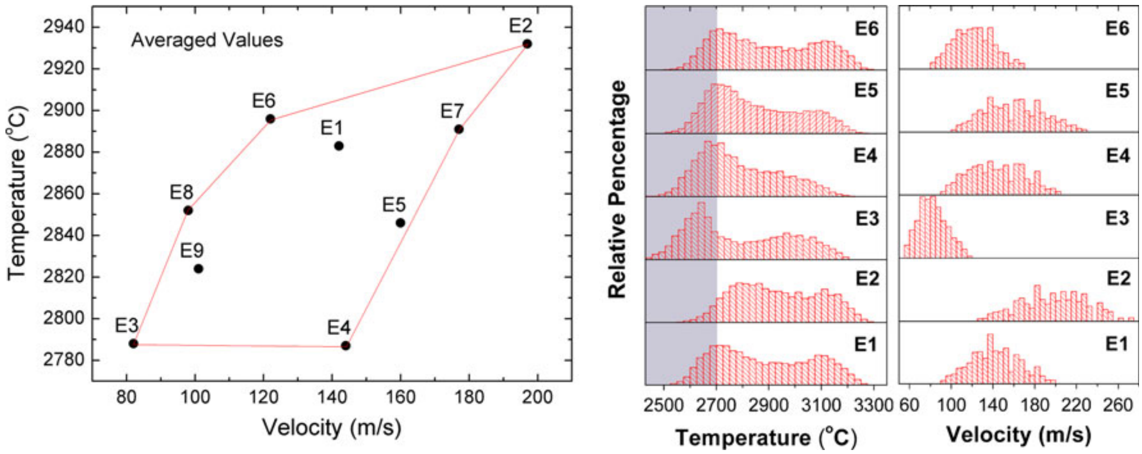

Fig. 3 Outcome of DoE-based process parameter selection on particle temperature and velocity at the spray distance 130 mm obtained via DPV-2000. Left: averaged *T*-*V* results represented in the form of a first-order process map; right: distribution of individual particle temperature and velocity. Shaded gray area in temperature distribution covers particles whose measured surface temperatures are below melting point

distribution of temperature and velocity of condition for E1 ~ E6 coatings. In the temperature plot, the shaded area represents temperature below melting point of YSZ (2690 °C). Many distributions show two peaks: one is around the melting point (latent heat plays the role here); the other is at above 3000 °C. It can be seen that a large portion of E3 particles are not well melted at the measurement point, while condition E2 particles are superheated. Velocity graph shows larger difference: most of E3 particles are below 120 m/s but all E2 ones are above it.

Variations of particle thermal and kinetic energies are evident from the T-V diagram (Ref 35-37). Particle temperature, velocity, and size distributions obtained using DPV for each process condition can be combined into group parameter descriptions of the particle states, namely, particle melting index (MI) and KE (Ref 38). MI is related to the ratio of particle residence time in the flame to the total time needed to melt the particle and is defined as $\mathrm{MI} = \frac{24k}{\rho h}\cdot\frac{1}{1+4/Bi}\cdot\frac{(T_{\mathrm{f}}-T_{\mathrm{m}})\cdot\Delta t}{D^2}$, where k is the thermal conductivity, ρ is the density of the material in liquid state, h is the enthalpy of fusion, T_{f} is the flame temperature near the in-flight particle, T_{m} is the melting point of the material, D is the particle size, and Bi is the Biot number. KE is defined as $\mathrm{KE} = \frac{1}{2}\,\mathrm{mV}^2$, where m is the mass of particle and V is the particle velocity.

A first-order process map based on MI and KE is shown in Fig. 4, where three zones can be observed with respect to particle melting. A low MI cluster comprises runs E3 and E4; while conditions E2 and E6 show much higher degree of melting. Left graph of Fig. 4 only shows the average MI and KE values, right two graphs show the distributions of individual particles. It is clear that all conditions contain some of unmelted particles, but E3 and E4 had more of them as compared to those with higher melting indices.

3.2 Splat Morphology and Coating Microstructure Characterization

Coatings were produced for carefully selected conditions shown in the first-order process map. They were deposited onto the in situ curvature sensor using procedures described in the ‘‘Materials and Methods’’ section. Coating thickness and weights were monitored for each process condition and relative deposit efficiencies were assessed from them across the spectrum of measured particle states (since all process conditions were kept constant).

Single splat morphologies provide a frame of reference for microstructural analysis (Ref 39, 40). Figure 5 compares these splat morphologies represented within the first-order process map. Near-perfect disk-shape splat morphologies were obtained for E3 coating. Similar results were identified for E4 with the exception of somewhat increased fragmentations along the periphery. This is attributable to increased KE of the particles due to the higher particle velocity (82 m/s compared to 144 m/s while average temperature is almost the same around 2788 °C). This fragmentation concerns the material excess in the periphery of the splat). It was also noted that these splats in some cases contain unmelted nodules within the splat indicative of partial melting of the particle. This observation is also corroborated with microstructures of the sprayed coatings. The E3 morphology has a distinctive appearance consisting of successive dense zones interrupted by large and long cracks probably originating from the stacking of these well-formed circular lamellae while cracks could have been produced to minimize thermal strains in the coating during built up.

YSZ coating microstructures (polished cross sections) were observed by SEM in the backscattered electron mode. A series of 15 images was recorded to get representative porosity values with a standard deviation as low

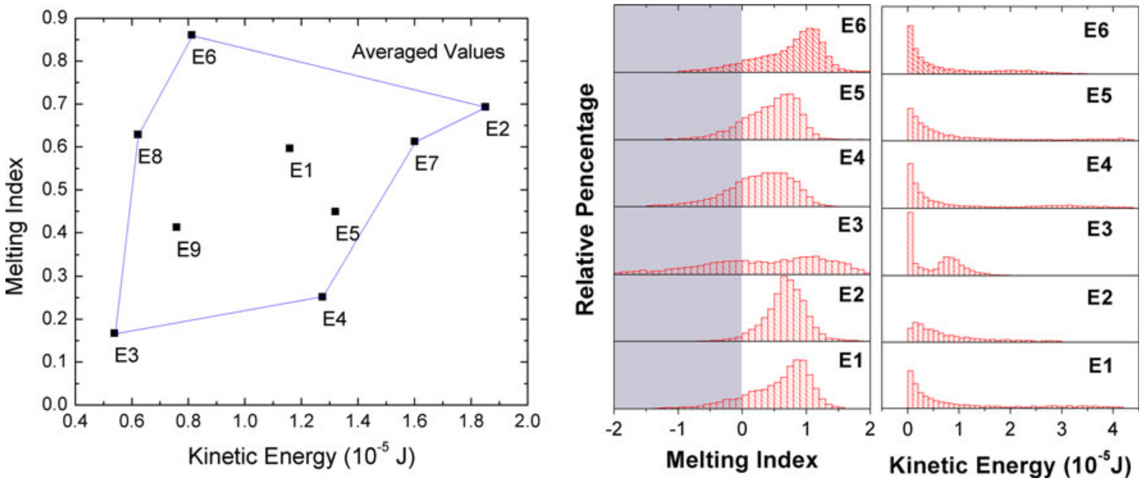

Fig. 4 The corresponding relationship expresses in terms of group parameters, namely MI and KE. Left: averaged results represented in the form of a first-order process map; right: distribution of individual particle MI and KE. Shaded gray area in MI distribution represents unmelted zone

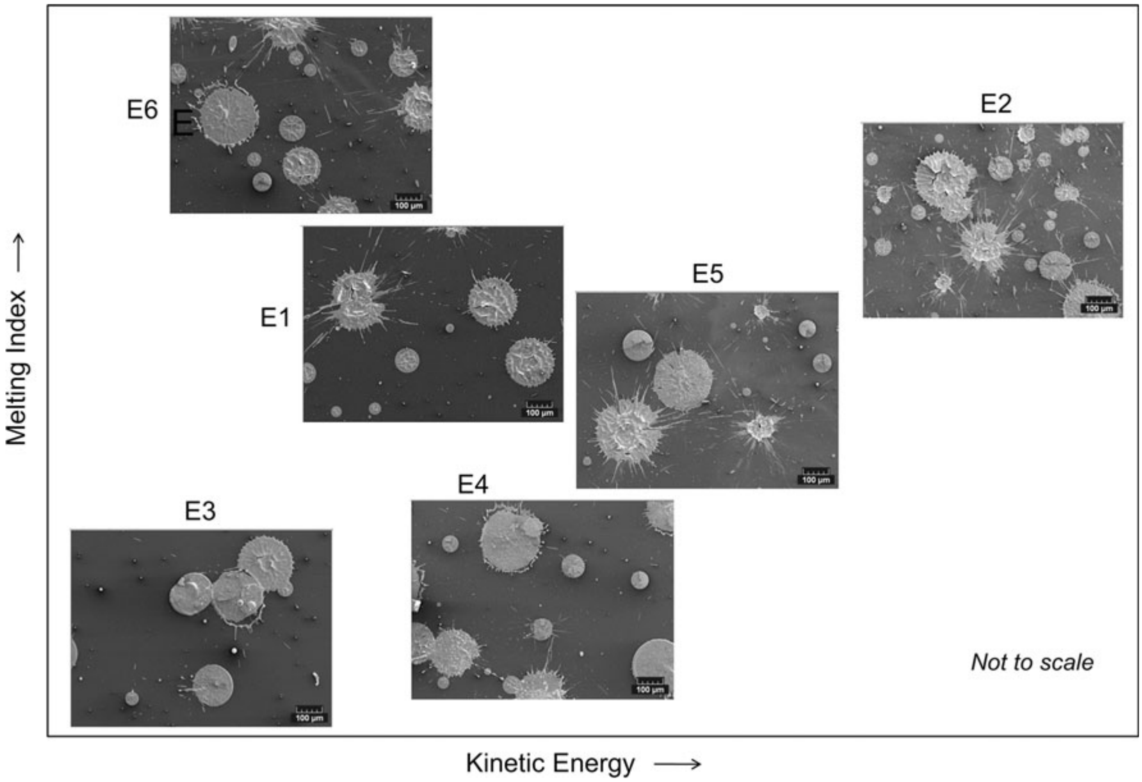

Fig. 5 Splat morphology for various spray parameter locations as represented within the framework of an MI-KE first-order process map

Table 2 Image analysis of the coating microstructures and computed porosity including delineation of types of porosity

Coating reference	Total porosity, vol.%	Macroporosity, vol.%	Microporosity, vol.%	Total crack length <30°, µm
E1	14.7	6.5	8.4	31,354
E2	15.3	5.7	9.8	33,882
E3	15.9	9.1	7.0	26,661
E4	18.0	10.3	7.8	26,487
E5	15.3	6.6	8.8	31,645
E6	14.2	6.1	8.4	28,039

as 1%. Image analysis was implemented to characterize the coating microstructure and the measurements are reported in Table 2 for each coating and microstructures are shown in Fig. 6.

Two coatings referenced as E3 and E4 are significantly different from the rest of the coatings. These coatings have been produced by lower MI. They have unique morphologies with estimated macroporosities of 9-10%, which is distinctly above the values achieved for the other coatings with ~6%. The porous network of E3 coating can be described as large and long cracks or interlaminar separations, whereas for E4 as depicted in Fig. 6, comprised numerous globular pores and partially melted particles incorporated into the coating. Coating E4 had the largest extent of total porosity. Particularly noteworthy is E3 sprayed at lower MI and lower KE than condition E2. Here, the overall porosity of the two conditions is similar but the difference between macroporosity and microporosity is significant.

Coatings referenced as E1, E2, E5, and E6 have in general similar lower macroporosity ratios (about 6.0-6.5 vol.%) compared to E3 and E4, and develop somewhat higher microporosities (from 8.5 to 10 vol.%) that are mainly microcracks. The overall total crack length oriented below 30° is also higher (Table 2).

In contrast to the observations made for E3 and E4, the splat morphologies shown in Fig. 5 for E2 and E5 are characterized by a high level of fragmentation resultant from increased MI and KE of the particles (Ref 38). For moderate MI values (for example E5 as shown in the first-order process map) it was noticed that splat shape changes from round circular to fragmented (splashed) with an increase of the particle size. For E2, a heterogeneous splat structure appears in the core of the splat indicative of

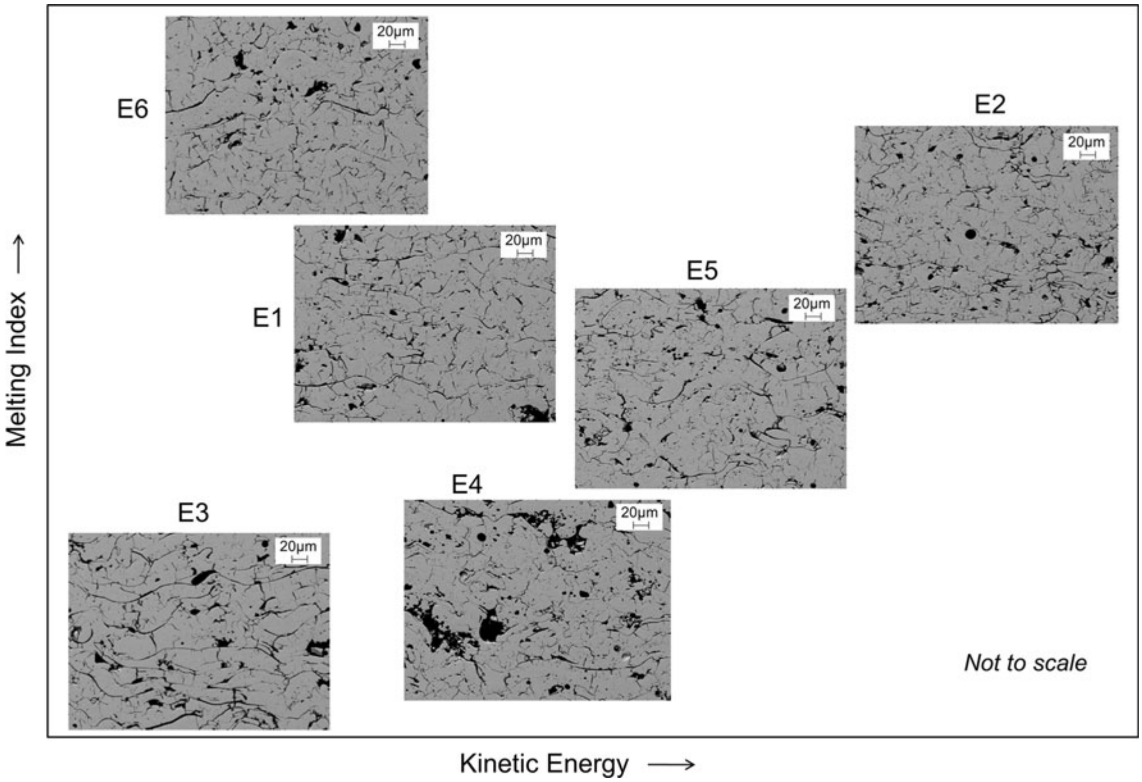

Fig. 6 SEM micrographs of the cross-sectional images for coatings fabricated at different processing conditions from E1 to E6, as represented within the framework of an MI-KE first-order process map

potential inner material ejection at these conditions. The evolution of splash or fragmentation between E4 (lower splat splashing), E1 or E5, and E2 (higher splat splashing) coincide with an increase of the microcrack ratio (from 7.8, 8.8, 8.4 to 9.8%).

These results demonstrate that it is feasible to produce plasma-sprayed TBCs with substantially different porosities and microstructures through judicious selection of process conditions. They must be effectively monitored and mapped through in situ particle diagnostics. In the next section, the implications of such microstructural tailoring on properties are addressed.

3.3 Ambient and Temperature-Dependent Thermal Conductivity for As-Sprayed and Aged TBCs

YSZ thermal conductivity values are sensitive to microstructural defect features, presented in the form of pores, intersplat, and interlaminar cracks, all of which contribute to the total porosity of the coating. The ambient gases within the defects which are less thermally conductive, along with the interface scattering to the conductive and radiative heat transfer, are believed to be the major reasons of the low plasma-sprayed TBC thermal conductivity compared to the bulk material as well as coatings produced by other processes. Heat treatment at elevated temperatures (>1000 °C) induces sintering and consequently changes the coating thermal conductivity (Ref 41-43). This section provides studies of YSZ thermal conductivity in terms of microstructure changes induced by processing conditions and thermal exposures.

Table 3 lists the ambient thermal conductivity of various coatings measured via room temperature laser flash technique of free-standing samples, for as-sprayed and thermally exposure TBCs with both cyclic and isothermal conditions. The thermal conductivity properties follow the distinct microstructural differences among the variously processed samples. Conditions E3 and E4 are representing the low MI regimes with the lowest thermal conductivity at ambient temperature. High MI conditions E6 and E2 fabricated coatings with the highest thermal conductivity; while conditions E5 and E1 were processed with moderate MI and corresponding coatings have intermediate conductivity. The general tendency indicates increasing thermal conductivity with increasing MI of the in-flight particles.

Table 3 also shows the ambient-temperature thermal conductivity before and after cyclic and isothermal exposures, which provides information on the microstructural stability during thermal aging. Two thermal exposure scenarios are represented: cyclic (20 cycles at 1100 °C, 30 min each) and isothermal (for an equivalent hot time of 10 h at 1200 °C). In general, thermal exposure increases coating thermal conductivity due to microstructural interface removal, i.e., sintering, especially at isothermal conditions (Ref 44). Cyclic exposures at high temperature also increase thermal conductivity due to sintering. However, during heating and cooling, additional microcracking

Table 3 Coating ambient thermal conductivity for as-sprayed and thermally exposure TBCs for both cyclic and isothermal conditions

		After cyclic aging		After isothermal aging	
Coating reference number	As-sprayed thermal conductivity, W/m · K	Thermal conductivity, W/m · K	Relative increase, %	Thermal conductivity, W/m · K	Relative increase, %
E1	1.05 ± 0.02	1.19 ± 0.02	13	1.19 ± 0.02	13
E2	1.08 ± 0.01	1.28 ± 0.01	19	1.31 ± 0.02	21
E3	0.83 ± 0.01	0.90 ± 0.02	8	0.95 ± 0.02	14
E4	0.88 ± 0.01	0.97 ± 0.02	10	1.03 ± 0.02	17
E5	1.05 ± 0.01	1.18 ± 0.03	12	1.20 ± 0.02	14
E6	1.19 ± 0.02	1.35 ± 0.03	13	1.36 ± 0.02	14

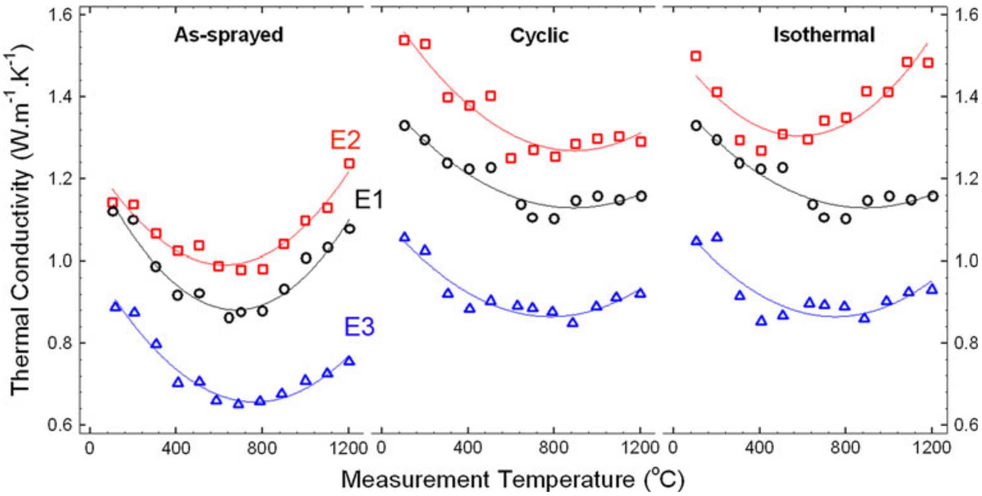

Fig. 7 Thermal conductivity at various temperatures for as-sprayed and thermally exposed (under cyclic and isothermal conditions) E1, E2, and E3 coatings. Laser flash measurement were performed every 100 °C up to 1200 °C in furnace

may occur, and results show a higher or similar conductivity values compared to isothermal conditions, although the cyclic aging was performed at lower temperature (1100 vs. 1200 °C). The net change in thermal conductivity between the two sets of aged samples for different starting samples is also shown. It is clear that E3 displays an overall lower sintering rate of 8 and 14%, respectively, for the two annealing conditions which is lower than most samples. Samples sprayed at high velocity and temperatures, e.g., E2 shows the most rapid sintering rate of all the samples indicating that the intersplat and interparticle contact is much stronger at these conditions.

TBCs are usually used at high temperatures to provide thermal insulation to metallic components. Thus, their thermal conductivities at high temperatures are important to evaluate TBC thermal performance. Figure 7 shows the temperature-dependent thermal conductivity results of E1, E2, and E3 coatings, which are representative conditions of high, medium, and low MI, respectively. The temperature-dependent thermal conductivity also increased after cyclic and isothermal exposures. The isothermal cases show similar increases to that of cyclic conditions. With respect to MI, same as the ambient results, the coating thermal conductivity at elevated temperature is higher with higher MI, as can be seen in Fig. 7. For as-sprayed, the thermal conductivity increases rapidly at temperatures above 800 °C, which is primarily due to two reasons: increase radiative heat transfer and in situ sintering during measurement. Such changes are much smaller for cyclic and isothermal aged samples, suggesting lesser effects of in situ aging. One exception is condition E2-isothermal: the sharp increase at high temperature indicates removal of interfaces during sintering. Condition E2 has been processed at high MI of in-flight particles, and exhibits less sintering resistance than E1 and E3.

3.4 Nonlinear Elastic Properties

Following the procedure by Liu et al. (Ref 24), concurrent monitoring of curvature changes with temperature under low temperature thermal cycle is used to extract the nonlinear elastic properties of E1-E6 coatings. The YSZ coatings were deliberately sprayed on aluminum substrates since the thermal mismatch strains from the ambient to 250 °C is in the same range as that of between YSZ and superalloy exposed to much higher temperatures (>900 °C).

To characterize the nonlinear elastic behavior without the influence of coating thickness, the curvature-temperature data are processed to determine the stress-strain relations using an inverse analysis (Ref 45). The results shown in Fig. 8 illustrate significant differences in strain-stress relations among various samples. For example, coating E3 sprayed at much lower plasma conditions (low MI) shows significantly more compliant response compared to the other conditions. Liu et al. further described these nonlinear relations in the form of two representative parameters namely the elastic modulus at low strain (representing a linear portion of the curve) and a second parameter, ''Nonlinear Degree'' (ND), which is introduced to quantify the extent of nonlinearity as: $\mathrm{ND} = E/E^{*}_{0.001}$. Here E is the room temperature elastic modulus and $E_{0.001}{}^{*}$ is the *secant* modulus between the transitional point (σ_T, ε_T) and the stress and strain at $\varepsilon = \varepsilon_T + 0.001$. The transitional point corresponds to the location where the stress-strain relation changes from linear to nonlinear (Ref 24). With this definition, a large ND value signifies greater nonlinearity while $\mathrm{ND} = 1$ if a coating remains linear elastic throughout the loading. The parameter essentially represents the departure of stress-strain relation from its initial linear slope. Table 4 lists the two parameters quantifying the nonlinear behavior of the various specimens as computed from such an analysis. The results clearly point to differences among the specimens both in terms of stiffness (as represented by the Young's modulus) and the extent of nonlinearity captured by the ND parameter. It is emphasized that that these values closely correlate with the microstructures of coatings. For examples, E3 and E4 coatings with large macroporosities (Table 2) exhibit low elastic modulus but higher nonlinearities. Samples with relatively large microporosities and total crack length (E1, E2, and E5) show stiffer responses (i.e., large E) and less nonlinearity (i.e., lower ND). It is also noted here that intra-splat cracks that believed to contribute to the nonlinearity is not accounted in the total crack length shown in Table 2. First they are generally oriented >30° and many may be filled in during polishing due to their thin or no openings. Further interpretation of the differences with respect to the process conditions is elaborated in the following section.

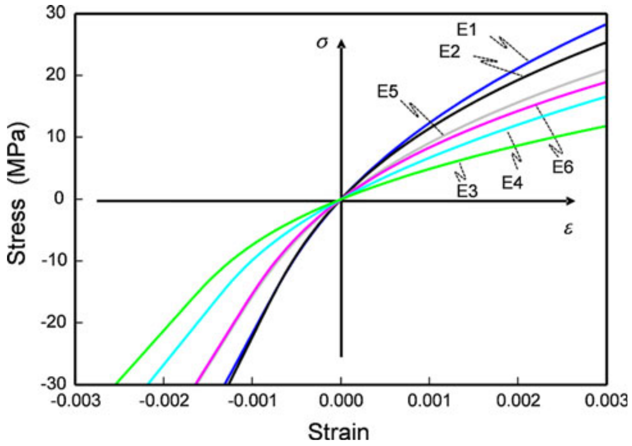

Fig. 8 Nonlinear stress-strain relations of various samples. They are determined by processing curvature-temperature data obtained by ECP (ex situ coating property) sensor during low temperature thermal cycles

Table 4 Coating elastic parameters, elastic modulus, and nonlinear degree of samples E1-E6

Coating reference	Elastic modulus, GPa	Nonlinear degree
E1	27.1	1.73
E2	27.2	1.71
E3	17.8	2.12
E4	18.8	1.94
E5	22.0	1.66
E6	24.6	1.88

4. Synthesis of Results and Integrated Analysis

This study provides an opportunity to integrate advances in materials and process science with novel approaches to characterization of complex layered materials such as plasma-sprayed YSZ TBCs. The opportunity to use controlled powders further facilitates careful delineation of process-microstructure-property relations and provides a framework for controlled introduction of thermal and elastic properties to TBC coatings. To further elucidate the observed process-property correlations, in this section, synthesis of second-order process maps is envisioned to link the critical process parameters with property outcomes.

As a first step, the particle state relations in Fig. 4 can be divided into three zones representing low, medium, and high melting indices of the particles, as shown in Fig. 9(a). This representation provides a framework for further discussion on the implications of particle properties on coating properties. For example, Fig. 9(b) is shown through the two mechanical parameters, E and ND, indicating remarkable correlations between the process conditions and the resulting coating mechanical properties. For each sample, its relative positions in two separate maps are consistent. For an example, E3 coatings made under lower temperature and velocity conditions exhibits low modulus and large nonlinearity.

Several important observations can be made:

4.1 Splat Morphology and Microstructure

In general, splats produced at nominally higher MI results in increased fragmentation (or splashing) which can lead to enhanced microporosity in the system. Data from Table 2 to a first approximation supports this finding as samples E3 and E4 shows reduced fragmentation. For similar MI increases in KE results in increased fragmentation and in the same vein, for similar KE, increasing MI results in greater fragmentation. Samples sprayed at low MI show only marginally higher total porosity (due to reduced fragmentation-induced microporosity) but much higher macroporosity (due to interlaminar separations). Samples E3 and E4 are thus substantially different than the other four samples.

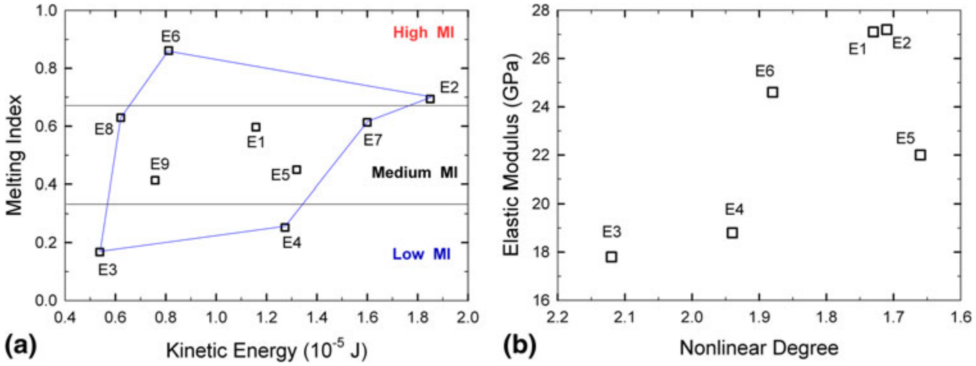

Fig. 9 (a) MI and KE process map, this is divided into three zones: high melting, med melting, and low melting; (b) Nonlinear degree versus elastic modulus for coatings E1-E6

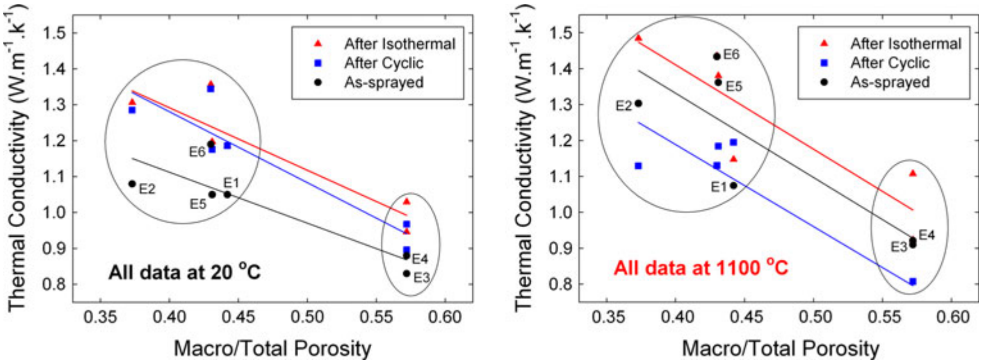

Fig. 10 As-sprayed coating thermal conductivity, measured by ambient laser flash, as well as the values which show increases after cycling and isothermal heat treatment: as a function of Macro/Total porosity. Left: measured at 20 °C; right: measured at 1100 °C

4.2 Microstructure and Thermal Conductivity

The ambient temperature thermal conductivity of the samples is significantly influenced by the type of microstructure influenced by the processing conditions. The results from Table 2, 3, and Fig. 7 are combined as Fig. 10 to represent the appropriate thermal conductivity porosity relations. Samples E3 and E4 which represents the low MI region of the process map associated with higher content of macroporosity with respect to total porosity shows generally lower thermal conductivity well below the industry norm of 1.0 W/m · K for APS YSZ. More subtle correlations on the impact of KE on ambient temperature thermal conductivity are difficult to interpret based on the given set of data. Thermal conductivity is in general more difficult to measure and is prone to higher uncertainties.

The temperature-dependent thermal conductivity also shows an overall similar response, i.e., to say coatings made with low MI generally show overall lower temperature-dependent thermal conductivity in both the as-sprayed and annealed states. At moderate-to-high MI parameters, the distinctions are more difficult to interpret. At these conditions, the pore architectures are more similar in terms of the fraction of macroporosity within the overall porosity. Since radiation becomes a much more dominant factor at elevated temperatures both measurement and interpretation of the microstructural dependencies can be more complicated. Nevertheless certain general conclusions can be drawn from the process which points to identification of processing conditions that will not only yield an impressive initial conductivity of value of ~0.8 W/m · K but also can provide enhanced resistance to sintering due to higher content of macroporosity in the system. The combination of lower KE and low MI captured in the E3 parameter points to achieving such microstructural control.

4.3 Thermal Conductivity and Elastic Properties

The nonlinear elastic properties from the stress-strain relations described in Fig. 9 and Table 4 provide two characteristic variables describe the coating compliance and also allows for mapping the effects of processing parameters. Figure 11 plots the relationship of the three important parameters, thermal conductivity, Young's modulus and nonlinear in elastic modulus. Coatings processed under low MI conditions (E3 and E4) show markedly lower stiffness (elastic modulus), generally higher nonlinear degree and lower thermal conductivity, while coatings produced with higher MI produce stiffer coatings. These two coatings with low MI are located in distinctly different locations within the parametric maps indicative of the significant microstructural differences arising from processing conditions. Within each regime,

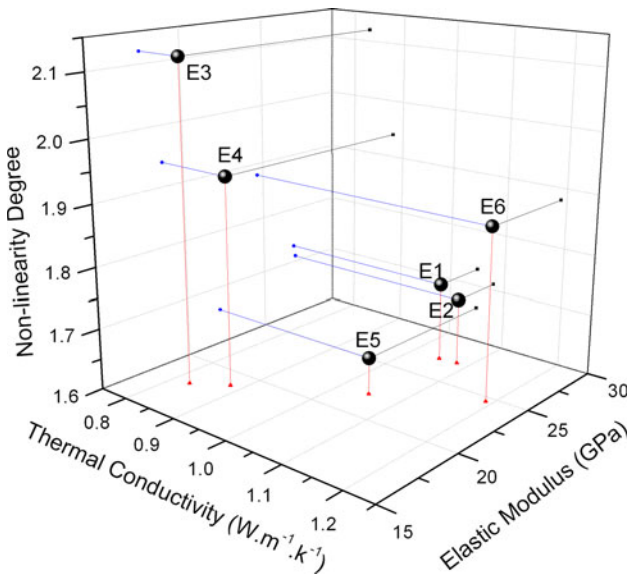

Fig. 11 3D map with coating thermal and elastic properties, in terms of *k*-*E*-ND relationships

the effect of particle KE is also noted. With the exception of E5, in general higher KE the degree of nonlinearity tends to decrease as shown in Fig. 11. It is noted that the second mechanical parameter (i.e., nonlinear degree) enables to establish the more precise correlations between the manufacturing processes to the actual coating behaviors. First-order parameters, such as elastic modulus or the thermal conductivity, are not sufficient to reveal the accurate effects of process conditions.

5. Conclusions

This paper presents results of an integrated study combining carefully designed hollow powders with controlled processing excursions to produce YSZ coatings with a diversity of microstructures. The principle strategy involved a DoE-based synthesis of first-order process maps which allowed coatings to be fabricated at different particle temperatures and velocities. They are more suitably expressed through the recently identified framework of group parameters, namely particle MI and KEs. These group parameters allow a more appropriate description of individual particles melting and kinetic states.

The results indicate that both MI and KEs of the particle affect the deposit formation as evidenced through droplet fragmentation during impact and contribute to variegated forms of porosity in the microstructures (Ref 46). In general, materials made at low MI show reduced propensity for fragmentation (splashing) and thus reduced microporosity in the coating. However, this is compensated by enhanced interlamellar porosity or macroporosity due to reduced flattening and spreading. The combined effect results in coatings with substantially reduced thermal conductivity and elastic modulus.

The above presented integrated relationships represented in terms of first- and second-order process maps provide a framework for microstructural control via processing towards optimizing critical properties of importance to YSZ TBCs notably conductivity and compliance. Combined with controlled powders, it is feasible to produce tailored microstructures with substantially lower thermal conductivity than generally reported for YSZ-TBC. An added benefit of such microstructural tailoring is the ability to also simultaneously enhance thermo-structural compliance and reduce propensity to sintering during elevated temperature exposure. The concepts developed in this paper can also be extended to emerging class of new TBC systems including zirconates where the additional opportunities for layered microstructural engineering are presented to address multiplicity of failure mechanisms such as erosion, foreign object damage, and CMAS attack.

Acknowledgments

This work was supported by the National Science Foundation GOALI program under award CMMI-1030492. The support of the industrial Consortium for Thermal Spray Technology is gratefully acknowledged. We acknowledge Dr. H. Wang at Oak Ridge National Laboratory and Dr. W. Chi for their valuable discussion.

References

1. C.G. Levi, Emerging Materials and Processes for Thermal Barrier Systems, *Curr. Opin. Solid State Mater. Sci.*, 2004, **8**(1), p 77-91
2. R.A. Miller, Current Status of Thermal Barrier Coatings—An Overview, *Surf. Coat. Technol.*, 1987, **30**(1), p 1-11
3. N.P. Padture, M. Gell, and E.H. Jordan, Thermal Barrier Coatings for Gas-Turbine Engine Applications, *Science*, 2002, **296**(5566), p 280-284
4. A.G. Evans, D.R. Mumm, J.W. Hutchinson, G.H. Meier, and F.S. Pettit, Mechanisms Controlling the Durability of Thermal Barrier Coatings, *Prog. Mater Sci.*, 2001, **46**(5), p 505-553
5. X.Q. Cao, R. Vassen, and D. Stoever, Ceramic Materials for Thermal Barrier Coatings, *J. Eur. Ceram. Soc.*, 2004, **24**(1), p 1-10
6. D.R. Clarke and C.G. Levi, Materials Design for the Next Generation Thermal Barrier Coatings, *Annu. Rev. Mater. Res.*, 2003, **33**, p 383-417
7. S. Sampath, Thermal Sprayed Ceramic Coatings: Fundamental Issues and Application Considerations, *Int. J. Mater. Product Technol.*, 2009, **35**(4), p 425-448
8. G. Antou, G. Montavon, F. Hlawka, A. Cornet, C. Coddet, and F. Machi, Evaluation of Modifications Induced on Pore Network and Structure of Partially Stabilized Zirconia Manufactured by Hybrid Plasma Spray Process, *Surf. Coat. Technol.*, 2004, **180-81**, p 627-632
9. C.A. Johnson, J.A. Ruud, R. Bruce, and D. Wortman, Relationships Between Residual Stress, Microstructure and Mechanical Properties of Electron Beam-Physical Vapor Deposition Thermal Barrier Coatings, *Surf. Coat. Technol.*, 1998, **108-109**, p 80-85
10. P. Bengtsson and T. Johannesson, Characterization of Microstructural Defects in Plasma-Sprayed Thermal Barrier Coatings, *J. Therm. Spray Technol.*, 1995, **4**(3), p 245-251
11. D.M. Zhu and R.A. Miller, Thermal Conductivity and Elastic Modulus Evolution of Thermal Barrier Coatings under High

Heat Flux Conditions, *J. Therm. Spray Technol.*, 2000, **9**(2), p 175-180

12. A. Vaidya, V. Sirinivasan, T. Streibl, M. Friis, W. Chi, and S. Sampath, Process Maps for Plasma Spraying of Yttria-Stabilized Zirconia: An Integrated Approach to Design, *Optim. Reliab. Mater. Sci. Eng. A*, 2008, **497**(1-2), p 239-253
13. G. Bertrand, P. Bertrand, P. Roy, C. Rio, and R. Mevrel, Low Conductivity Plasma Sprayed Thermal Barrier Coating Using Hollow Psz Spheres: Correlation between Thermophysical Properties and Microstructure, *Surf. Coat. Technol.*, 2008, **202**(10), p 1994-2001
14. H.B. Guo, S. Kuroda, and H. Murakami, Microstructures and Properties of Plasma-Sprayed Segmented Thermal Barrier Coatings, *J. Am. Ceram. Soc.*, 2006, **89**(4), p 1432-1439
15. A. Kulkarni, Z. Wang, T. Nakamura, S. Sampath, A. Goland, H. Herman, J. Allen, J. Ilavsky, G. Long, J. Frahm, and R.W. Steinbrech, Comprehensive Microstructural Characterization and Predictive Property Modeling of Plasma-Sprayed Zirconia Coatings, *Acta Mater.*, 2003, **51**(9), p 2457-2475
16. Z. Wang, A. Kulkarni, S. Deshpande, T. Nakamura, and H. Herman, Effects of Pores and Interfaces on Effective Properties of Plasma Sprayed Zirconia Coatings, *Acta Mater.*, 2003, **51**(18), p 5319-5334
17. W. Chi, S. Sampath, and H. Wang, Microstructure-Thermal Conductivity Relationships for Plasma Sprayed Yttria Stabilized Zirconia Coatings, *J. Am. Ceram. Soc.*, 2008, **91**(8), p 2636-2645
18. Y. Tan, J.P. Longtin, S. Sampath, and H. Wang, Effect of the Starting Microstructure on the Thermal Properties of as-Sprayed and Thermally Exposed Plasma-Sprayed YSZ Coatings, *J. Am. Ceram. Soc.*, 2009, **92**(3), p 710-716
19. H.E. Eaton, J.R. Linsey, and R.B. Dinwiddie, The Effect of Thermal Aging on the Thermal Conductivity of Plasma Sprayed Fully Stabilized Zirconia, *Thermal Conductivity*, Vol 22, T. Tong, Ed., Technomic Pub, Lancaster, 1994, p 289-300
20. Y. Tan, J. Longtin, S. Sampath, and H. Wang, Effect of the Starting Microstructure on the Thermal Properties of as-Sprayed and Thermally Exposed Plasma-Sprayed YSZ Coatings, *J. Am. Ceram. Soc.*, 2009, **92**, p 710-716
21. P. Roy, G. Bertrand, and C. Coddet, Spray Drying and Sintering of Zirconia Based Hollow Powders, *Powder Technol.*, 2005, **157**(1-3), p 20-26
22. G. Bertrand, P. Roy, C. Filiatre, and C. Coddet, Spray-Dried Ceramic Powders: A Quantitative Correlation between Slurry Characteristics and Shapes of the Granules, *Chem. Eng. Sci.*, 2005, **60**(1), p 95-102
23. H. Mahdjoub, P. Roy, C. Filiatre, G. Bertrand, and C. Coddet, The Effect of the Slurry Formulation Upon the Morphology of Spray-Dried Yttria Stabilised Zirconia Particles, *J. Eur. Ceram. Soc.*, 2003, **23**(10), p 1637-1648
24. Y. Liu, T. Nakamura, V. Srinivasan, A. Vaidya, A. Gouldstone, and S. Sampath, Non-Linear Elastic Properties of Plasma-Sprayed Zirconia Coatings and Associated Relationships with Processing Conditions, *Acta Mater.*, 2007, **55**(14), p 4667-4678
25. G. Mauer, R. Vassen, and D. Stover, Plasma and Particle Temperature Measurements in Thermal Spray: Approaches and Applications, *J. Therm. Spray Technol.*, 2011, **20**(3), p 391-406
26. S. Sampath, V. Srinivasan, A. Valarezo, A. Vaidya, and T. Streibl, Sensing, Control, and in Situ Measurement of Coating Properties: An Integrated Approach toward Establishing Process-Property Correlations, *J. Therm. Spray Technol.*, 2009, **18**(2), p 243-255
27. M. Vardelle, P. Fauchais, A. Vardelle, K. Li, B. Dussoubs, and N. Themelis, Controlling Particle Injection in Plasma Spraying, *J. Therm. Spray Technol.*, 2001, **10**(2), p 267-284
28. V. Srinivasan, M. Friis, A. Vaidya, T. Streibl, and S. Sampath, Particle Injection in Direct Current Air Plasma Spray: Salient Observations and Optimization Strategies, *Plasma Chem. Plasma Process.*, 2007, **27**(5), p 609-623
29. J. Matejicek and S. Sampath, In Situ Measurement of Residual Stresses and Elastic Moduli in Thermal Sprayed Coatings—Part 1: Apparatus and Analysis, *Acta Mater.*, 2003, **51**(3), p 863-872
30. Y.C. Tsui and T.W. Clyne, An Analytical Model for Predicting Residual Stresses in Progressively Deposited Coatings. 1. Planar Geometry, *Thin Solid Films*, 1997, **306**(1), p 23-33
31. Y. Tan, J.P. Longtin, and S. Sampath, Modeling Thermal Conductivity of Thermal Spray Coatings: Comparing Predictions to Experiments, *J. Therm. Spray Technol.*, 2006, **15**(4), p 545-552
32. Y. Tan, J. Longtin, and S. Sampath, Modeling Thermal Conductivity of Thermal Spray Coatings: Comparing Predictions to Experiments, *J. Therm. Spray Technol.*, 2006, **15**, p 545-552
33. G. Dwivedi, T. Nakamura, and S. Sampath, Controlled Introduction of Anelasticity in Plasma-Sprayed Ceramics, *J. Am. Ceram. Soc.*, 2011, **94**, p s104-s111
34. Y.J. Liu, T. Nakamura, G. Dwivedi, A. Valarezo, and S. Sampath, Anelastic Behavior of Plasma-Sprayed Zirconia Coatings, *J. Am. Ceram. Soc.*, 2008, **91**(12), p 4036-4043
35. M. Vardelle, A. Vardelle, P. Fauchais, and C. Moreau, Pyrometer System for Monitoring the Particle Impact on a Substrate During a Plasma Spray Process, *Meas. Sci. Technol.*, 1994, **5**(3), p 205-212
36. G. Mauer, R. Vaßen, and D. Stöver, Detection of Melting Temperatures and Sources of Errors Using Two-Color Pyrometry During in-Flight Measurements of Atmospheric Plasma-Sprayed Particles, *Int. J. Thermophys.*, 2008, **29**(2), p 764-786
37. G. Mauer, R. Vaßen, and D. Stöver, Comparison and Applications of Dpv-2000 and Accuraspray-G3 Diagnostic Systems, *J. Therm. Spray Technol.*, 2007, **16**(3), p 414-424
38. W. Zhang and S. Sampath, A Universal Method for Representation of In-Flight Particle Characteristics in Thermal Spray Processes, *J. Therm. Spray Technol.*, 2009, **18**(1), p 23-34
39. L. Bianchi, A.C. Leger, M. Vardelle, A. Vardelle, and P. Fauchais, Splat Formation and Cooling of Plasma-Sprayed Zirconia, *Thin Solid Films*, 1997, **305**(1-2), p 35-47
40. K. Shinoda, H. Murakami, S. Kuroda, K. Takehara, and S. Oki, In Situ Visualization of Impacting Phenomena of Plasma-Sprayed Zirconia: From Single Splat to Coating Formation, *J. Therm. Spray Technol.*, 2008, **17**(5), p 623-630
41. F. Cernuschi, L. Lorenzoni, S. Ahmaniemi, P. Vuoristo, and T. Mantyla, Studies of the Sintering Kinetics of Thick Thermal Barrier Coatings by Thermal Diffusivity Measurements, *J. Eur. Ceram. Soc.*, 2005, **25**(4), p 393-400
42. A. Cipitria, I.O. Golosnoy, and T.W. Clyne, A Sintering Model for Plasma-Sprayed Zirconia TBCs. Part I: Free-Standing Coatings, *Acta Mater.*, 2009, **57**(4), p 980-992
43. S. Tsipas, I. Golosnoy, T. Clyne, and R. Damani, The Effect of a High Thermal Gradient on Sintering and Stiffening in the Top Coat of a Thermal Barrier Coating System, *J. Therm. Spray Technol.*, 2004, **13**(3), p 370-376
44. N. Markocsan, P. Nylén, J. Wigren, X.H. Li, and A. Tricoire, Effect of Thermal Aging on Microstructure and Functional Properties of Zirconia-Base Thermal Barrier Coatings, *J. Therm. Spray Technol.*, 2009, **18**(2), p 201-208
45. T. Nakamura and Y. Liu, Determination of Nonlinear Properties of Thermal Sprayed Ceramic Coatings via Inverse Analysis, *Int. J. Solids Struct.*, 2007, **44**(6), p 1990-2009
46. M. Vardelle, A. Vardelle, A.C. Leger, P. Fauchais, and D. Gobin, Influence of Particle Parameters at Impact on Splat Formation and Solidification in Plasma Spraying Processes, *J. Therm. Spray Technol.*, 1995, **4**(1), p 50-58